Chemical Geology
March 2020, Volume 537 Pages 119481 (13p.)
https://doi.org/10.1016/j.chemgeo.2020.119481
https://archimer.ifremer.fr/doc/00606/71799/

Large nickel isotope fractionation caused by surface complexation reactions with hexagonal birnessite

Sorensen Jeffry V. [1], Gueguen Bleuenn [2, 3, 4], Stewart Brandy D. [1], Peña Jasquelin [5], Rouxel Olivier [4], Toner Brandy M. [1, *]

[1] University of Minnesota-Twin Cities, MN 55108, USA
[2] CNRS, Univ Brest, UMR 6538 Laboratoire Géosciences Océan, F-29280 Plouzané, France
[3] CNRS, Univ Brest, UMS 3113, F-29280 Plouzané, France
[4] IFREMER, Centre de Brest, Unité Géosciences Marines, F-29280 Plouzané, France
[5] Institute of Earth Surface Dynamics, University of Lausanne, CH-1015 Lausanne, Switzerland

* Corresponding author : Brandy M. Toner, email address : toner@umn.edu

Abstract :

Manganese oxides are an important sink for Ni in the ocean. To explore the potential of Ni stable isotopes as a geochemical tracer, we conducted two types of sorption reactions between Ni and hexagonal birnessite in 0.05 M $NaNO_3$ media: one where we varied pH from 5 to 8 (constant initial Ni concentration = 170 μmol/L), and a second where we varied the initial dissolved Ni concentration from 17 to 426 μmol/L (constant pH = 7.7). Isotopic measurements were made on both the solid phase and the supernatant solutions to determine the Ni isotope fractionation factors (Δ60/58Nimin-aq = δ60/58Nimin − δ60/58Niaq) between the mineral and aqueous phases. Nickel extended X-ray absorption fine structure (EXAFS) spectroscopy showed Ni in two distinct bonding environments: one where Ni atoms incorporate into the MnO_2 sheet and a second where Ni atoms associate with the mineral surface sharing oxygens with 3 Mn tetrahedra (TCS, triple corner sharing). As pH and net negative surface charge increase, the coordination of Ni shifts to higher proportions of incorporation. The number of structural vacancies in birnessite, which are locations for TCS coordination of Ni, are controlled by pH and increase with decreasing pH. These vacancies are preferentially occupied by lighter Ni isotopes leading to fractionation factors, Δ60/58Nimin-aq, ranging from −2.76‰ (lowest TCS) to −3.35‰ (maximum TCS). These Ni isotopic fractionation factors are among the largest observed in natural geological and biological materials to date. Our findings reveal a relationship between Ni coordination environment and pH that may ultimately be used as an isotopic geochemical tracer of past ocean conditions. However, the results are inconsistent with current isotopic fractionation factors for marine ferromanganese deposits relative to seawater and point to unaddressed processes that modify Ni isotopic fractionation for ferromanganese deposits. Further research is needed to develop Ni as an isotopic tracer.

Highlights

►Manganese oxides are important nickel sink in oceans. ► Nickel exists in two distinct chemical bonding environments with manganese oxide birnessite. ► Both nickel surface bonding and nickel birnessite mineral incorporation forms exist. ► Nickel isotopic fractionation between aqueous phase and solid birnessite occurs. ► Future potential for nickel as geochemical tracer of past ocean conditions.

Keywords : Ni stable isotope fractionation, Ni EXAFS, Surface complexation, Birnessite, Tracer development

1. Introduction

Over geological time scales, variations in Ni bioavailability in the ocean may have impacted the global carbon cycle (Konhauser et al., 2009; Rothman et al., 2014). In the modern ocean, Ni is an important biologically-active trace metal and essential micronutrient for marine phytoplankton. Nickel has a nutrient-type profile showing depletion in surface waters due to consumption by biological activity and enrichment in deep waters due to recycling of organic matter in the water column (Bruland, 1980; Feller et al., 1991; Morel et al., 2003; Morel and Price, 2003). The dominant sources of Ni to the ocean are rivers, and potentially hydrothermal vents and atmospheric dusts, with concentrations in seawater ranging from 2 to 12 nmol/L (Boyle et al., 1981; Bruland, 1980; Cameron and Vance, 2014; Sclater et al., 1976). Surface seawater concentrations are relatively high compared to other transition metals even in phosphate-depleted surface seawater, most likely due to enhanced solubility of organically-bound Ni (Mackey et al., 2002). From a biogeochemical perspective, Ni sources and sinks within the ocean are heavily dependent on geochemical reactions between Ni and minerals, combined with organic matter cycling (Cameron and Vance, 2014; Vance et al., 2016).

Evidence to-date suggests that scavenging of Ni by Mn (oxyhydr)oxides is an important control on the biogeochemical cycling of Ni in both marine and terrestrial environments, thus providing a major pathway for Ni removal (i.e., sink) from seawater (Cameron and Vance, 2014; Gall et al., 2013; Gueguen et al., 2016; Vance et al., 2016). Nickel has been observed to partition from seawater to Mn and Fe (oxyhydr)oxide phases including minerals formed in-situ in pelagic sediments, Fe-Mn crusts and nodules, and metalliferous deposits (Bonatti et al., 1972; Bostrom and Peterson, 1966; Cronan, 2000; Nicholson and Eley, 1997). In particular, a systematic correlation between Ni and Mn has been reported for metalliferous deposits such as

marine ferromanganese nodules and crusts (Aplin and Cronan, 1985; Koschinsky and Halbach, 1995; Koschinsky and Hein, 2003; Peacock, 2009), as well as Fe- and Mn-(oxyhydr)oxides in soils (Chukhrov et al., 1981; Manceau et al., 2002b). The incorporation of metals, including Ni, in Fe- and Mn-(oxyhydr)oxide phases is generally assumed to occur via sorption reactions onto the mineral surface. As demonstrated for other trace metals elements, such as, B (Lemarchand et al., 2007), Tl (Nielsen et al., 2013), Zn (Pokrovsky et al., 2005), Ge(Pokrovsky et al., 2014), Mo (Barling and Anbar, 2004; Kashiwabara et al., 2011), Cd(Wasylenki et al., 2014) and U (Brennecka et al., 2011), sorption processes might produce an isotopic offset in Ni relative to seawater.

Recent experimental studies report that sorption and co-precipitation reactions yield measurable stable isotopic signatures for Ni (Fujii et al., 2011; Gueguen et al., 2018; Wasylenki et al., 2015). For example, Ni in the mineral phase is isotopically lighter following sorption onto Fe oxyhydroxide ferrihydrite (~ -0.35 ‰) (Wasylenki et al., 2015). In a follow-up study, Gueguen et al. 2018 found that Ni sorption on goethite (α-FeOOH) produced an even more fractionated sorbed-Ni with enrichment of the solid phase in light Ni isotopes by -0.77 ‰. Nickel extended X-ray absorption fine structure (EXAFS) data on these samples indicated that the difference in Ni isotope fractionation extent between ferrihydrite and goethite is related to the degree of Ni coordination at the mineral surface. Specifically, the number of Fe atoms coordinating each Ni atom (in the second-shell) was lower for goethite than for ferrihydrite. This observation was interpreted as a weaker surface complex between goethite and Ni that favored adsorption of isotopically light Ni.

The present study provides a first assessment of the extent of Ni isotope fractionation during sorption on Mn (oxyhydr)oxides—as a function of pH and Ni-loading to the mineral

hexagonal birnessite—in the context of detailed mineral structure and surface coordination chemistry as measured by Ni and Mn EXAFS.

2. Methods

2.1 Mineral synthesis and characterization

Hexagonal-birnessite ($K_{0.5}Mn_2O_4 \cdot 1.5H_2O$, also known as "acid birnessite") was prepared by boiling a 2.5 L solution of 0.4 mol/L $KMnO_4$ with vigorous mechanical stirring. The precipitate was formed through dropwise addition of 163 mL of concentrated HCl using a burette. The precipitate was then washed in 3 centrifuge-resuspend cycles with purified water (18.2 M MΩ; MilliQ), separated from suspension using vacuum filtration (0.22 µm Millipore polyethersulfone), and finally freeze dried and stored as a dry powder (McKenzie, 1971; Villalobos et al., 2003). All reagents were ACS (American Chemical Society) grade. The purity of the powder was confirmed by powder X-ray diffraction.

The surface area of the birnessite powder was measured (after degassing at 150 ^oC), with a Quantachrom Quantasorb analyzer via N_2 adsorption. The calculated BET surface area was 36.12 m^2/g (Brunauer et al., 1936).

Zeta potential measurements were conducted using a ZetaPALS analyzer (Brookhaven Instruments Corp.) by suspending birnessite particles in purified water (18.2 MΩ; MilliQ) at a concentration of 1.52 g/L and averaged from 3 cycles of 5 runs each. The samples were analyzed using a conductance of 82 µS, a current of 0.34 mA, applied voltage of 7.54V, and an electric field of 9.29 V/cm. The zeta potential measurements at pH 7 show that birnessite exhibits a negative surface charge of -55.41 mV.

Elemental composition of the birnessite ($K_{0.5}Mn_2O_4 \cdot 1.5H_2O$) was determined by ICP-MS (Inductively coupled plasma Mass Spectrometer) on a Thermofisher Scientific X-Series instrument with an ESI PC3 Peltier cooled spray chamber, SC-FAST injection loop, SC-4 autosampler, and an internal Yttrium standard (Geochemistry Laboratory, Department of Earth Sciences, University of Minnesota Twin Cities).

2.2 Sorption experiments

Nickel sorption experiments were based on published methods for Ni adsorption on Fe oxyhydroxide minerals (Gueguen et al., 2018). Ni stock solution (17.04 mmol Ni/L) was prepared with $Ni(NO_3)_2 \times 6H_2O$ (MW= 290.71). All experiments began by preparing six 250 mL Teflon reaction vessels (Nucleopore) by adding a 0.075-0.150 g of birnessite (dry weight) to 150 mL of 0.05 mol/L $NaNO_3$ electrolyte solution. Sodium nitrate was chosen as the electrolyte, over NaCl, because NO_3^- aq forms fewer aqueous complexes with Ni^{2+} aq than would Cl^- aq. Throughout the experiment the suspensions were continuously mixed using Teflon-coated magnetic stir bars and pH was controlled by automated titration with 0.05 mol/L HNO_3 or 0.05 mol/L NaOH. pH was monitored and adjusted with a custom-built pH control system consisting of 6 Hanna Instruments HI 504 controllers each with a Thermo Scientific Orion 9110 pH electrode. pH adjustments were made with proportional additions of 0.05 mol/L HNO_3 and 0.05 mol/L NaOH using two 3-way General Valve solenoid valves and a Manostat Carter peristaltic cassette pump, the system provided pH control of ± 0.2 pH units. Adsorption experiments were conducted as functions of Ni loading (0 to 0.852 µmol Ni/kg suspension) and pH (5.0-8.2) at 25°C. These reaction conditions were chosen to mimic the environmental conditions and Ni loadings observed in ferromanganese deposits (Peacock, 2009; Peacock and Sherman, 2007a)

(Peacock and Sherman, 2005). Experiment 1 was performed as a function of pH (pH 5.0, 6.0, 7.0, 7.7, 8.0, and 8.2) with an initial Ni concentration of 170 µmol/L Ni. Experiment 2 was performed as a function of initial Ni concentration (17, 85, 170, 341, and 426 µmol/L) at pH 7.7. After addition of Ni, the suspension was agitated using a magnetic stir bar at 25°C and allowed to react for 24 hours before the solution was separated from the solids by vacuum filtration (0.22 µm polycarbonate, Millipore). The supernatant solution was refrigerated until analysis by ICP-MS and the solid material (filter-bound paste) was stored frozen. Solid Ni-sorbed mineral samples were split for EXAFS and isotopic analysis.

The aqueous speciation of Ni was calculated for the experimental conditions using MINEQL+ v.4.6 (Environmental Research Software) with stability constants from NIST (NIST, 1995). Calculations used initial Ni concentrations of 17, 85, 170, 341, and 426 µmol Ni/L, pH range of 5.0 to 8.0, ionic strength of 0.05 mol/L $NaNO_3$, and partial pressure of CO_2 of 94.3 ppm for an open system. Nickel precipitates were not predicted to form under our experimental conditions.

2.3 Extended X-ray absorption fine structure (EXAFS) spectroscopy

Nickel K-edge EXAFS spectra were collected at the Advanced Photon Source (Argonne National Laboratory) beamline 20-BM in fluorescence mode. The Mn K-edge EXAFS were collected in transmission mode at beamline 20-BM. Due to limited instrument time, Ni and Mn EXAFS spectra were not collected for all sorption experiments. Nickle EXAFS spectra were collected for samples having a pH range of 5.0 – 8.2, and a Ni loading range of 21.5 – 254 µmol Ni / g birnessite. Manganese EXAFS spectra were collected for birnessite equilibrated at pH 7.0, 7.7, 8.0, and 8.2, but not for the two lower pH conditions (pH 5.0 and 6.0).

Samples were prepared for EXAFS analysis by thawing and transferring, as a thin smear, to Kapton adhesive. Multiple layers of sample were stacked and sealed with Kapton adhesive. Measurements were conducted at room temperature. Individual scans were examined for changes in peak position or shape to detect photon-induced sample alteration; none were observed. The monochromator energy was calibrated using a Ni metal foil and set to 8334.5 eV or a Mn metal foil at 6537.67 eV. Two detectors were used: (1) a liquid-nitrogen-cooled 12-element Canberra Germanium [Ge(Li)] detector for fluorescence mode measurements and (2) an in-line transmission ion chambers for reference measurements.

All EXAFS data processing was done using the IFEFFIT software suite with the Athena program used for energy calibration, pre-edge subtraction, and post-edge normalization (Ravel and Newville, 2005). Shell-by-shell fitting was accomplished using the SixPack software package (Webb, 2005). Fitting the Ni-O shell of $NiCl_2$(aq) and Ni(II)EDTA(aq) was used to determine an amplitude reduction factor (S^2_0) of 0.96 (Pena et al., 2010). Threshold energy (ΔE_0) was allowed to vary but was linked for all shells during fitting. For all fits the bond distance (R), coordination number (CN), and the Debye-Waller factor (σ^2) were allowed to vary for each path, unless otherwise stated. All paths were generated using the FEFF6L program from SixPack and the mineral structure data for birnessite (Post and Veblen, 1990).

A model for the Ni EXAFS data was created by fitting the Ni-O first-shell contributions and fixing them while fitting the second-shell. The second-shell was modeled with two Ni-Mn paths corresponding to Ni incorporation into the mineral and Ni in a triple corner sharing (TCS) orientation (Manceau et al., 2007b; Peacock, 2009; Pena et al., 2010). To fit the two Ni-Mn paths, we linked the Ni-Mn1 path (Ni incorporated) to the Ni-Mn2 path (TCS) by defining the variable (F) to represent the fraction of the Ni in the TCS coordination. The coordination number

for TCS sites was expressed as 6 × F and as 6 × (1-F) for the incorporated Ni. During the fitting process, the total number of Ni-Mn pairs was constrained to a value of 6. Linking the two second-shell paths with shared variable F allowed us to determine the ratio of Ni incorporated into the mineral versus Ni in a TCS orientation.

The statistical parameters of R-factor (value of 0.05 or less being an acceptable value) and reduced chi square (reduced χ^2), both calculated by IFEFFIT, were used to determine the quality of shell-by-shell fits. In addition, the uncertainty of fitted parameters generated by FEFF6L (Kelly et al., 2008) and visual inspection of the fit in k-space and the Fourier-transform, including the imaginary portion, were used to evaluate the goodness of fit.

2.4 Chromatographic column purification of nickel

Birnessite samples were dissolved in 10 mL of 6 mol/L HCl for 72 hours at room temperature. Dissolution was complete and did not require any heating. Prior to chromatographic column separation, elemental concentrations of Ni, Fe and Mn were measured by quadrupole ICP-MS (X-Series 2, Thermofisher Scientific) at the Pôle Spectrométrie Océan (PSO, Laboratoire Géosciences Océan, Brest, France). The fraction of Ni adsorbed was determined by mass balance using the initial Ni concentration in solution and the amount of Ni measured in minerals after the experiment.

The method employed for separating Ni isotopes from the matrix using ion-exchange chromatographic columns, is described in Gueguen et al. (2013) and summarized here. Briefly, a fixed aliquot of the archive solution in 6 mol/L HCl was collected and loaded on an anion-exchange chromatographic column using AG1-X8 anion exchange resin (Biorad) for removing traces of Fe. A second separation step involving a Ni-specific resin (Eichrom) in which Ni forms

a complex with dimethylglyoxime, ensured purification of Ni from remaining matrix elements such as Mn from birnessite and Na from the electrolyte. Aliquots of the supernatant solutions and the Ni stock solution were only processed through the Ni-specific resin while splits of birnessite were processed through the entire chemical procedure (Gueguen et al., 2013).

2.5 Mass spectrometry procedure and double-spike correction scheme

Nickel isotope compositions were measured by MC-ICP-MS Neptune (Thermofisher Scientific) at PSO, Ifremer (Brest, France) using a double-spike (mixture of ^{61}Ni and ^{62}Ni isotopes) added to samples prior to loading on Ni-specific resin (2nd step of chromatography columns separation) to correct for instrumental mass bias. An Apex Q (Elemental Scientific, USA) desolvation introduction system was employed and Ni isotopes were measured in high resolution mode to resolve argide interferences. The double-spike correction scheme of isotope ratios was computed using an iterative method as described in (Siebert et al., 2001). The double-spike was added in a known amount with a spike/natural concentration ratio of 1 as described by Gueguen et al. (2013) (Gueguen et al., 2013). Analysis of each sample on the mass spectrometer consists of 50 cycles of measurement for which we calculated an internal two standard error value (2se) that is typically in the range of 0.02 and 0.05 ‰. Based on duplicated isotope analysis of Ni standard solution and georeferenced materials (e.g., BHVO-2, Nod-A-1, Nod-P-1), we determined a long-term external precision (2 standard deviation) of about 0.06 ‰. The $\delta^{60/58}$Ni values obtained for the geostandards are 0.03 ±0.06 ‰, 1.04 ±0.04 ‰ and 0.34 ±0.03 ‰ for BHVO-2, Nod-A-1 and Nod-P-1 respectively, consistent with previously published values.

The Ni isotope composition of sorbed and aqueous Ni are reported according to the conventional delta notation (1) using the Ni international isotopic standard NIST SRM 986 as the

reference standard ratio ($R_{NIST986}$) and the Ni isotope ratio of the sample (R_{sample}) for $^{60}Ni/^{58}Ni$ following the approach of Gueguen et al. (Gueguen et al., 2013):

$$\delta^{60/58}Ni\ (‰) = (R_{sample}/R_{NIST986} - 1) \times 1000 \qquad (1)$$

3. Results

3.1 Nickel sorption

Table 1 shows the range of values observed for the percent Ni sorbed ($Ni_{mineral}/Ni_{intial} \times 100\%$) to birnessite for the pH gradient (constant Ni) experiment ranging from 59.5% to 100 % and for the concentration gradient (constant pH) experiment ranging from 64.0% to 100%. The final loading of Ni to birnessite ranged from 221.8 to 249.7 µmol Ni/g mineral (2.01-2.27 µmol Ni/mol Mn) for the pH gradient experiment and from 21.5 to 225.0 µmol Ni/g mineral (0.20-2.04 umol Ni/mol Mn) for the concentration gradient experiment (Figure 1).

3.2 Nickel EXAFS spectroscopy

Shell-by-shell fitting was performed for all Ni EXAFS spectra (Table 2, Figure 2). All spectra were fit with ~ 6 Ni-O atom pairs in the first-shell at a distance of 2.04 ± 0.01 Å. The second-shell was fit by linking two Ni-Mn paths, one at ca. 2.86 Å (Ni incorporated into the MnO_2 sheet) and the other at ca. 3.49 Å (Ni in triple corner sharing coordination at a vacancy site (TCS)), which combined have ~ 6 Ni-Mn atom pairs. The Ni k-edge spectra for the pH-gradient samples (Figure 2b) show systematic changes in the EXAFS spectra near k=8 $Å^{-1}$ consistent with a change in the average Ni-Mn bonding environment as pH increases, consistent with less Ni in TCS configuration. A comparison of two samples with different Ni loadings and consistent pH (Figure 2c) for pH 6, 7, and 8 shows that increased Ni concentration causes less splitting in the

oscillation of the spectral features between k=9-11 $Å^{-1}$. The Ni k-space spectra for the concentration gradient samples (Figure 2a) do exhibit systematic changes as Ni concentration increases. Fourier transforms (FTs) of the spectra for all samples are presented in Supplementary Information (Figure S1). These images show two clear coordination environments for Ni sorption, Ni incorporated into the mineral sheet at $R+\Delta R$ =2.5 and Ni in a TCS configuration at $R+\Delta R$ =3.2 (Peña et al., 2010).

By linking the second-shell Ni-Mn paths via the F variable it was possible to determine that the percentage of Ni in the TCS coordination ranged from 69% to 95% across all samples. For the pH gradient samples (Table 2), the percentage of Ni in the TCS coordination shows a trend of decreasing TCS as a function of increasing pH: 95% TCS at pH 5 to 80% TCS at pH 8.2. The concentration gradient samples (at pH 7.7) show a more subtle trend of increasing TCS with increased Ni loading to the mineral: 78% at 21 µmol Ni/g mineral to 86 % at 190 µmol Ni/g mineral. The samples NiBirn_pH50_C227 (pH 5 with final loading of 227 µmol Ni/g birnessite) and NiBirn_pH60_C234 (pH 6 with final loading of 234 µmol Ni/g birnessite) exhibit Ni incorporation into the birnessite sheets on the order of 5-10 % of total sorbed Ni (1-F) (Table 2). The error estimate for the F variable is ± 3-10 %. Fitting the Ni-incorporated shell is thus difficult and required the σ^2 value for the TCS shell to be set at 0.005 in order to accomplish fitting.

3.3 Manganese EXAFS spectroscopy

Manganese K-edge EXAFS spectra were collected for birnessite following reaction with Ni over a range of pH values. Figure 3 shows that no changes were observed in the Mn EXAFS as pH increased. Comparison to the findings of Villalobos for unaltered hexagonal birnessite

from the same synthesis protocol shows matching EXAFS spectral features (Villalobos et al., 2006). These factors indicate there was no detectable change (with EXAF90ykS) in the structure of birnessite due to changes in pH during the experiments.

3.4 Nickel isotope compositions

Nickel isotope measurements were performed on both the solid phase and the supernatant solution following sorption experiments for the pH gradient experiments at 0.075 g of mineral and for the solid phase only for the concentration gradient experiments and pH gradient experiments at 0.15 g of mineral (Table 1). The initial Ni stock solution was processed through chromatographic separation and yielded a Ni isotope composition of $\delta^{60/58}Ni_{initial}$ -0.32 ±0.06 ‰ (n=3, 2sd). The Ni isotope fractionation factor $\Delta^{60/58}Ni_{min\text{-}aq}$ for the sorption experiments is expressed as the apparent difference in Ni isotopic composition between the mineral-sorbed Ni and Ni remaining in solution (2):

$$\Delta^{60/58}Ni_{min\text{-}aq} = \delta^{60/58}Ni_{mineral} - \delta^{60/58}Ni_{aqueous} \quad (2)$$

Mass balance considerations also imply that:

$$\delta^{60/58}Ni_{initial} = [\%ads \times \delta^{60/58}Ni_{mineral} + (100- \%ads) \times \delta^{60/58}Ni_{aqueous}]/100 \quad (3)$$

where %ads is the percentage of Ni adsorbed onto birnessite. By combining equations (2) and (3), it is possible to calculate the fractionation factor (4) for the "concentration gradient" experiments for which the $\delta^{60/58}Ni_{aqueous}$ values were not determined, insofar as %ads is

significantly different from 0% or 100% as it is the case for Ni_Birn_pH77_C189 and Ni_Birn_pH77_C190 (Table 1).

$$\Delta^{60/58}Ni_{min\text{-}aq} = [\delta^{60/58}Ni_{mineral} - (\delta^{60/58}Ni_{initial} - \%ads \times \delta^{60/58}Ni_{mineral})/(100- \%ads)]/100 \quad (4)$$

Results are presented in Table 1 and Figure 4. Isotopic mass balance of the system (equation 3) was verified for the "pH gradient experiment set 2" and yielded $\delta^{60/58}$Ni values identical within uncertainty to the Ni isotope composition of the initial Ni stock solution. Birnessite minerals efficiently scavenge Ni from solution. Sorption experiments with low Ni in solution (17, 85 and 170 µmol/L of Ni) show complete (>99 %) Ni sorption onto the mineral surface and thus the Ni isotope composition of the aqueous phase could not be determined for these samples. However, the average Ni isotope composition of the mineral phases is -0.33 ± 0.09 ‰ (2sd, n=3), similar, within uncertainty, to the $\delta^{60/58}$Ni value of the initial Ni stock solution (-0.32 ±0.06 ‰, 2sd). These results are consistent with total scavenging of $Ni_{(aq)}$ onto the birnessite surface. For the concentration dependent experiments that did not show complete uptake of Ni from solution (from 64 to 71 %), we determined the fractionation factor values $\Delta^{60/58}Ni_{min\text{-}aq}$ using the mass balance equation (3) and results show $\Delta^{60/58}Ni_{min\text{-}aq}$ values at -2.43 ± 0.28‰ (2sd, n=2).

The pH gradient experiments at 0.15g of birnessite per reactor (set 1) show total sorption of aqueous Ni, thus $\Delta^{60/58}Ni_{min\text{-}aq}$ values could not be calculated. The average Ni isotope composition of the solid phases is -0.34 ±0.03 ‰ (2sd, n=4) consistent with the Ni isotope composition of the initial stock solution. For pH gradient experiment at 0.075g of birnessite per reactor (set 2), the Ni sorption range from 59 to 68% and the $\delta^{60/58}$Ni values of the solid phases

range from -1.53 ± 0.03 ‰ to -1.41 ±0.02 ‰ and the Ni isotope composition of the associated supernatant solutions varied from +1.33 ±0.03 ‰ to +1.94 ±0.04 ‰ (Table 1, Figure 5). The isotope fractionation factor between the mineral and the solution for the pH-dependent experiments indicate enrichment of the mineral phase in light Ni isotopes compared to the aqueous phase, with $\Delta^{60/58}Ni_{min\text{-}aq}$ values ranging from -3.35 ±0.05 ‰ to -2.76 ±0.04 ‰ and yielding an average of -2.99 ±0.41 ‰ (2sd, n=7) (Table 1, Figure 6).

4. Discussion

4.1 Mineralogical controls on Ni isotope fractionation

4.1.1 Structure of birnessite

Hexagonal or potassium birnessite is characterized as a layer-type Mn oxide exhibiting hexagonal sheet symmetry (Manceau et al., 2003; Silvester et al., 1997). It consists of sheets of edge-sharing Mn^{4+} octahedra that may have vacancies or Mn^{3+} substitution resulting in a negative layer charge (Lopano et al., 2009). Previous work by Lanson and Manceau (2002) attributed the layer charge of synthetic hexagonal birnessite to approximately 17% of the Mn sites in the sheet being vacant (Lanson et al., 2002; Manceau et al., 2002a). This layer charge is compensated for by protons and interlayer cations with each octahedral vacancy capped by a cation that could include Mn^{3+}.

In the present study, when Ni^{2+} is oriented above a surface vacancy it adopts an inner-sphere triple-corner-sharing surface complex (TCS) at a Ni-Mn interatomic distance of ~3.5 Å (Bodei et al., 2007; Manceau et al., 2002a; Peacock and Sherman, 2007b; Pena et al., 2010). Additionally, Ni has been found to be incorporated into the sheets of hexagonal birnessite in an

edge-sharing configuration with its neighboring Mn(IV) octahedral with an interatomic distance of ~2.9Å (Manceau et al., 2007a; Peacock, 2009; Peacock and Sherman, 2007b).

We observed no detectable change in the structure of birnessite due to changes in experimental pH, as shown in Figure 3, for pH 7.0 to 8.2. Previous work showed that changes in the birnessite structure can occur between pH 3.7 and 5 (Peacock, 2009; Peacock and Sherman, 2007a). This suggests that changes in birnessite structure can occur at low pH, and perhaps affect our two lowest pH values, 5.0 and 6.0. Therefore, the relationships we observe may not be applicable below pH 7. This indicates that changes in the location or amount of Ni sorption in the pH range 7.0 to 8.2 are not due to changes in the birnessite structure.

4.1.2 pH and concentration dependence of Ni sorption

We observed nearly complete adsorption of Ni to birnessite when the initial Ni concentration was 170 µmol/L with 0.15 g of mineral in 150 mL 0.05M $NaNO_3$ solution. (Table 1). Peacock (2007) observed near total adsorption of dissolved Ni under similar experimental conditions at pH 7 regardless of the time the solution was allowed to incubate (Peacock, 2009). When either the Ni concentration in our reactions was increased to 341 µmol/L or the amount of mineral was reduced to 0.075 g, adsorption decreased to between 60% and 71% while the total amount of Ni adsorbed to the mineral increased only slightly (Table 1). This pattern is illustrated in Figure 1b and represents an adsorption isotherm, which shows that the Ni loading approaches a maximum value of ~250 µmol of Ni per gram of mineral. Previous studies showed that increasing the concentration of dissolved Ni above 0.6 µmol/L does not significantly affect the total sorption of Ni (Langmuir, 1997; Peacock and Sherman, 2007a; Simanova et al., 2015). Toner et al. (2006) conducted similar experiments with Zn sorption to biogenic hexagonal

birnessite and reported a similar adsorption isotherm. However, those experiments did not reach the breakthrough concentration, which is likely due to the presence of microbial biomass (Toner et al., 2005; Toner et al., 2006).

Although the Ni coordination environment at the mineral surface changes as a function of pH, the total Ni loading to the mineral does not change (Figure 1a). Our results show that dissolved Ni concentration impacts the final Ni loading to birnessite until the cation sorption capacity of birnessite, which is controlled by pH driven surface charge, is reached. This information, paired with the knowledge that the structure of birnessite remains stable across the pH range investigated, shows that pH is the master variable in controlling these adsorption processes. One of the major findings of this study is that change in pH has a significant effect on the Ni isotope equilibrium fractionation factors. $\Delta^{60/58}Ni_{min\text{-}aq}$ values vary from -2.76 ‰ to -3.35 ‰ for pH values ranging from 8.2 to 7.0 showing that isotopically lighter Ni is sorbed at lower pH. The pH range investigated here includes that of seawater, which suggests that Ni isotopes could be used as paleo-pH proxy in seawater. Although these results are promising, they require additional experimental data on, for example, the effect of salinity (ionic strength of the experiments) on Ni isotope fractionation.

4.1.3 Nickel coordination chemistry

The Ni EXAFS data and fits obtained in this study are consistent with inner-sphere complexation of Ni by birnessite and with previous studies (Manceau et al., 2007a; Manceau et al., 2007b; Manceau et al., 2007c; Peacock and Sherman, 2007b; Pena et al., 2011; Pena et al.,

2010). The coordination environment of Ni is octahedral with the first shell consisting of 6 O at ~ 2.04 ± 0.01 Å. Previous EXAFS studies using laboratory generated minerals have reported first shells consisting of 6 O at a distance of 2.0±0.06 Å [43, 45, 56, 57, 62]. The second coordination shell is comprised of a total of six Mn atoms present at two distinct distances, 2.86±0.02 Å and 3.48±0.01 Å [43, 45, 56, 57, 62]. Previous work has identified these two distances as representing Ni which is incorporated into the mineral structure and Ni which is in a TCS orientation (Manceau et al., 2007b; Peacock, 2009; Pena et al., 2010). Based on the findings of Simanova et al. (2015) it is possible that a third coordination scenario in which Ni sorbs to edge sites on the birnessite may account for up to 10-20% of the surface-associated Ni; however, our EXAFS fit results do not provide evidence for this coordination environment (Simanova et al., 2015).

For laboratory generated Mn minerals, Peacock (2009) and Peña (2010) report second shell values for Ni consisting of 6 Mn at 3.5±0.1 Å and identify it as Ni complexes located on the surface of the Mn minerals (Peacock, 2009; Peacock and Sherman, 2007b; Pena et al., 2010). Our σ^2 values are in agreement with those reported in the studies discussed above. Studies on natural ferromanganese nodules and crusts also report similar values for the Ni coordination environment. Manceau (2002) reported a Ni-O distance of 2.05 Å and Ni-Mn distance of 2.91 Å for Ni in the Mn minerals of a soil nodule (Manceau et al., 2002b). Peacock (2007) found that the Ni present in nodule and crust samples from the Pacific Ocean exhibited 6 O at ~2 Å and 6 Mn at ~2.9 Å, and interpreted it as Ni incorporated into the Mn mineral structure (Peacock and Sherman, 2007a). In a study of a freshwater ferromanganese nodule, Manceau (2007) identifies Ni incorporated into the structure of birnessite at 2.91±0.01 Å and Ni complexes at vacant layer sites at 3.49±0.02 Å (Manceau et al., 2007a).

4.1.4. Nickel isotopic fractionation

Our study, along with several others, provides experimental evidence that Ni is incorporated into the mineral structure of layer-type Mn (oxyhydr)oxides over short time scales and that the resulting Ni speciation varies with pH (Bodei et al., 2007; Manceau et al., 2002a; Peacock and Sherman, 2007a). Here we used a dual isotopic-spectroscopic approach to quantify the change in *both* proportion of TCS coordination to mineral incorporation *and* isotopic fractionation factor, as a function of pH. We observe that the Ni isotope fractionation factor for Ni-loaded birnessite is correlated with coordination chemistry (Figure 6). Specifically, as pH increased from 7.0 to 8.2, the proportion of Ni in TCS coordination decreased. We observed greater Ni incorporation with increased pH; density functional theory calculations indicate this might be due to a pH-dependent energy barrier that decreases at higher pH leading to greater incorporation (Pena et al., 2010). We also observed an enrichment of heavier Ni isotopes associated with the mineral, as expressed by the $\Delta^{60/58}Ni_{min\text{-}aq}$ values increasing from -3.25 ‰ to -2.76 ‰ as pH increases from 7.0 to 8.2. These results are consistent with a pH-dependent change in the proportion of TCS and a pH-dependent change in isotope fractionation. While these observations do not demonstrate causality, an interpretation of our findings is that the isotopic fractionation response is due to the surface coordination chemistry, both of which are a function of the master variable pH.

There are large differences in Ni isotope fractionation factors for sorption on either Fe-(oxyhydr)oxides such as 2-line ferrihydrite and goethite (up to ~ -0.8 ‰) (Gueguen et al., 2018; Wasylenki et al., 2015), or Mn-(oxyhydr)oxides (up to ~ -3 ‰) (this study). The difference in Ni isotopic fractionation observed for the two types of minerals is critical for developing Ni isotopes

as a geochemical tracer. Iron-(oxyhdr)oxides are mostly relevant for weathering on continental surfaces (Ratie et al., 2015) while in marine environmentss Mn-(oxyhydr)oxides are the predominant phases controlling Ni uptake from seawater (Cameron and Vance, 2014; Ciscato et al., 2018; Gall et al., 2013; Gueguen et al., 2016). While each of these mineral groups harbor complexity, especially when loaded with trace metal impurities, we can draw some general and overarching conclusions about them. For example, we know that these mineral groups (i.e., Fe- versus Mn-(oxyhydr)oxides) have very different reactivity with cations based on their permanent and variable charge characteristics (Sposito, 1989). Iron-(oxyhydr)oxides, such as goethite, are characterized by variable (pH-dependent) charge and a net neutral or slight positive charge in seawater (e.g. PZNC of 7-8). In contrast, Mn-(oxyhydr)oxides such as birnessite (MnO_2) have both permanent (Mn vacancies) and variable charge characteristics with a strong net negative charge in seawater (e.g., PZNC of 1.5-2.5). Given these charge properties, we would expect Mn-(oxyhydr)oxides to have a stronger affinity for cations (such as Ni) than Fe-(oxyhydr)oxides, and direct observation supports this reasoning (Takahashi et al., 2007).

4.2. Implications for geochemical tracer development

Marine ferromanganese crusts, comprised of Fe and Mn-(oxyhydr)oxides, constitute one of the major Ni reservoirs in modern oceans. In contrast to the Ni sorption experimental results presented here, Ni isotopic fractionation between ferromanganese crusts and modern day seawater is not observed (Gall et al., 2013). This discrepancy points to unrecognized processes that affect Ni isotope fractionation and require investigation. Here we will discuss several types of processes that should be investigated further: reaction kinetics, coordination chemistry, aqueous Ni speciation, and partitioning of Ni into minerals other than Mn (oxyhydr)oxides.

It is possible that marine ferromanganese deposits reach isotopic equilibrium faster than new crust formation processes can preserve the initial isotopic signature. For example, experimental results from Cd sorption on birnessite show a decrease in Cd isotope fractionation factor values with duration of reaction from $\Delta^{114/112}$Cd ~0.4 ‰ after 1 hour to $\Delta^{114/112}$Cd ~0.1 ‰ after 912 hours (Wasylenki et al., 2014). The authors attributed this result to structural incorporation of Cd combined with a reversible sorption mechanism, allowing continuous isotopic exchange between the solution and the mineral. The fractionation factor determined between Fe-Mn crusts for Cd is similar to the 0.1 ‰ value determined for longer duration experiments (Horner et al., 2010; Schmitt et al., 2009). Building on the interpretation of Wasylenki et al. (2015), long exposure time of Fe-Mn crusts to seawater during slow formation of the crusts (a few mm/Ma) could explain the limited Ni isotope fractionation between seawater and Fe-Mn crusts (Wasylenki et al., 2015).

Another potential explanation for the observed difference between our laboratory results and Fe-Mn crust measurements is a difference in Ni coordination chemistry. While our samples are dominated by Ni in the TCS coordination, Ni associated with Fe-Mn crusts is largely incorporated into the mineral structure (Peacock and Sherman (2007b) which could give rise to a difference in isotopic signature. For example, Nielsen et.al (Nielsen et al., 2013) reported differences in isotopic fractionation during thallium sorption onto birnessite depending on whether sorption occurred in Mn vacancies (large fractionation) or on edge sites (negligible fractionation). The present study found two Ni coordination environments, sorption at vacancies and incorporation into the birnessite structure. The fractionation factors for these two different coordination environments could perhaps be investigated using a triclinic birnessite lacking vacancies as an experimental end-member (Lanson et al. 2002).

Aqueous Ni speciation is another potential influence on Ni isotope fractionation between Fe-Mn crusts and seawater, in particular, complexation reactions with organic ligands may be important. Owing to its relatively low charge to radius ratio, Ni commonly exists as a hydrated Ni^{2+} ion in aqueous settings (Gaillardet et al., 2014), with Ni^{2+} and $NiCl^{+}$ being the primary inorganic species in seawater (20 % and 57 %, respectively) (Fujii et al., 2011). However, measurements of Ni concentration in the Beaulieu estuary (UK) showed that Ni adsorption on inorganic detrital particles is limited when organic matter is present due to Ni-ligand complexation (Turner et al., 1998). Nimmo et al. (1989) reported that 31-41 % of dissolved Ni in the Liverpool Bay was organically bound. These findings indicate that organic ligands play a significant role in Ni speciation in seawater (Boiteau et al., 2016; Mackey, 1983; Mackey et al., 2002; Nimmo et al., 1989; Turner and Martino, 2006; Van den Berg and Nimmo, 1987). The potential impact of organic species on the isotopic composition of inorganic Ni in seawater was theoretically and experimentally explored by Fujii et al. (2011) (Fujii et al., 2011) where authors demonstrated that fractionations up to 2.5‰ for $\delta^{60/58}Ni$ could occur during exchange reactions between inorganic and organic ligands, while enrichment in heavy Ni isotopes likely occurs in the order of $Ni^{2+} > NiCl^{+} > NiCl_2$. It follows that if the $Ni^{2+}_{(aq)}$ species is preferentially sorbed on ferromanganese crusts (Koschinsky and Halbach, 1995) this could result in enrichment in heavy Ni isotopes compared to bulk seawater. A more complete understanding of the role of aqueous speciation, and in particular the impact of Ni-organic complexes and their influence on adsorption to mineral surfaces, will undoubtedly help to explain Ni isotope cycling in seawater,weathering environments, and its incorporation in marine sediments.

The geochemistry of the sediments in contact with seawater is also expected to exert control over Ni isotope fractionation. For example, Vance and others have demonstrated that

seawater associated with sulfide phases displays an isotopically heavy Ni signature as compared to the lighter signature of the associated sediments (Cameron and Vance, 2014; Vance et al., 2017; Vance et al., 2016). Laboratory studies comparing Ni partitioning to Fe and Mn oxides to Ni precipitation as a sulfide mineral should be a promising future research direction to develop the Ni isotope tracer for different oxidation-reduction regimes.

4.3 Conclusion

Nickel isotope fractionation factors ranging from -2.76 ‰ to -3.35 ‰, measured here during sorption of Ni on birnessite are among the largest observed for natural geological and biological materials to date (Cameron and Vance, 2014; Ciscato et al., 2018; Gall et al., 2013; Gueguen et al., 2013; Gueguen et al., 2016; Gueguen et al., 2018; Porter et al., 2014; Ratie et al., 2015; Vance et al., 2016; Wasylenki et al., 2015). In comparison, the magnitude of the fractionation factor resulting from Ni sorption onto ferrihydrite (-0.35 ‰) (Gueguen et al., 2018; Wasylenki et al., 2015) and goethite (-0.77 ‰) (Gueguen et al., 2018) is up to an order of magnitude smaller. It is possible that this appreciable difference in the fractionation between Fe-(oxyhydr)oxides and Mn-(oxyhydr)oxides during Ni sorption could result in large differences in Ni isotope signatures in natural systems depending on the specific mineral phases present. Additionally, the Ni isotope fractionation factor measured here is larger than Ni isotope fractionation driven by biotic processes, as illustrated by Ni uptake by methanogens (~ -1 ‰) (Cameron et al., 2009), and also between dissolved seawater species including organic and inorganic species (~ 2.5 ‰) (Fujii et al., 2011) and solids (Ciscato et al., 2018; Porter et al., 2014).

Prior to using Ni isotopic signatures as a window into past oceanic biogeochemical conditions there are several complicating factors, including reaction kinetics, fractionation factors for specific coordination chemistries, aqueous Ni speciation, and partitioning of Ni into minerals other than Fe and Mn (oxyhydr)oxides that must be more fully documented through laboratory experimentation. Additional studies are needed to render Ni isotopic signature a reliable means of geochemical tracer. Of particular note is the large discrepancy between the isotopic signature observed in this study and that of marine ferromanganese deposits in equilibrium with modern day seawater, which points to potential missing links in our current understanding of Ni marine biogeochemistry.

Acknowledgments

We thank the Kuehnast Endowment Fund (Department of Soil, Water & Climate, University of Minnesota) for research support (JVS); the National Science Foundation (1037991 to BMT); Rick Knurr for ICP-MS analyses (Geochemistry Laboratory, University of Minnesota); Dale Brewe, Steven Heald, and Mali Balasubramanian for assistance with EXAFS data collection (beamline 20-BM, Advanced Photon Source, Argonne National Laboratory); Lindsey Briscoe for the construction of the pH-stat system; Lee Penn (Department of Chemistry, University of Minnesota) for access to the zeta potential instrument; and Kyungsoo Yoo (Department of Soil, Water & Climate, University of Minnesota) for access to the BET instrument. The powder X-ray diffraction was conducted at the Characterization Facility, University of Minnesota. This research used resources of the Advanced Photon Source, a U.S. Department of Energy (DOE) Office of Science User Facility operated for the DOE Office of Science by Argonne National Laboratory under Contract No. DE-AC02-06CH11357.

Table Captions

Table 1. Sample information and summary of experimental conditions including Ni loading to the mineral, Ni isotope composition (‰) of mineral phases (for all experiments) and of supernatant solutions (for pH-dependent experiments).

Table 2. Optimized fit parameters for Ni extended X-ray absorption fine structure (EXAFS) spectra for all experimental samples.

Figure Captions

Figure 1. (a) Nickel sorption to birnessite at 170 µmol/L initial Ni concentration for pH conditions 5.0 to 8.2, and (b) Ni sorption to birnessite from 17 to 426 µmol/L initial Ni concentrations at pH 7.7.

Figure 2. Comparison of Ni extended X-ray absorption fine structure (EXAFS) k^3-weighted data and shell-by-shell fit results for samples from sorption experiments consisting of: (a) a pH gradient from pH 5 to 8.2; (b) a comparison of two samples at pH 6, 7, and 8 with different Ni loadings to birnessite; and (c) a concentration gradient at pH 7.7.Experimental data are solid lines and fits are dashed lines.

Figure 3. A comparison of Mn extended X-ray absorption fine structure (EXAFS) k^3-weighted data for birnessite in samples ranging from pH 7 to 8.2.

Figure 4. Nickel isotope composition (‰) of birnessite solid phases (circles) and supernatant solutions (squares) versus sorption percentage for pH-dependent experiments (black line indicates Ni isotope composition of the starting Ni solution ($\delta^{60/58}$Ni = -0.32 ‰)). Error bars show the two-standard error of the mean.

Figure 5. Nickel isotope fractionation factors ($\Delta^{60/58}Ni_{min\text{-}aq} = \delta^{60/58}Ni_{mineral} - \delta^{60/58}Ni_{aqueous}$) versus pH (A) and final Ni loading (B) to the mineral (µmol/g mineral) for pH-dependent experiments. With the exception of the data point at pH 6, other samples show a trend between higher pH and lower $\Delta^{60/58}Ni_{min\text{-}aq}$ values, i.e. lower isotope fractionation for Ni sorbed onto the mineral at higher pH. Error bars show the two-standard error of the mean.

Figure 6. Nickel isotope fractionation factors $\Delta^{60/58}Ni_{min\text{-}aq} = \delta^{60/58}Ni_{mineral} - \delta^{60/58}Ni_{aqueous}$) versus Ftcs, which corresponds to the proportion of total Ni in TCS coordination. pH values of each data point are shown on the plot. Error bars show the two-standard error of the mean.

References

Aplin, A.C., Cronan, D.S., 1985. Ferromanganese oxide deposits from the Central Pacific Ocean, II. Nodules and associated sediments. Geochimica et Cosmochimica Acta, 49: 437-451.
Barling, J., Anbar, A.D., 2004. Molybdenum isotope fractionation during adsorption by manganese oxides. Earth and Planetary Science Letters, 217(3-4): 315-329.
Bodei, S., Manceau, A., Geoffroy, N., Baronnet, A., Buatier, M., 2007. Formation of todorokite from vernadite in Ni-rich hemipelagic sediments. Geochimica et Cosmochimica Acta, 71(23): 5698-5716.
Boiteau, R.M. et al., 2016. Structural Characterization of Natural Nickel and Copper Binding Ligands along the US GEOTRACES Eastern Pacific Zonal Transect. Frontiers in Marine Science, 3.
Bonatti, E., Kramer, T., Rydekk, H., 1972. Classification and genesis of submarine iron-manganese deposits, Ferromanganese deposits on the ocean floor, pp. 117-122.
Bostrom, K., Peterson, M.N., 1966. PRECIPITATES FROM HYDROTHERMAL EXHALATIONS ON EAST PACIFIC RISE. Economic Geology, 61(7): 1258-&.
Boyle, E.A., Huested, S.S., Jones, S.P., 1981. ON THE DISTRIBUTION OF COPPER, NICKEL, AND CADMIUM IN THE SURFACE WATERS OF THE NORTH-ATLANTIC AND NORTH PACIFIC-OCEAN. Journal of Geophysical Research-Oceans, 86(NC9): 8048-8066.
Brennecka, G.A., Wasylenki, L.E., Bargar, J.R., Weyer, S., Anbar, A.D., 2011. Uranium Isotope Fractionation during Adsorption to Mn-Oxyhydroxides. Environmental Science & Technology, 45(4): 1370-1375.
Bruland, K.W., 1980. OCEANOGRAPHIC DISTRIBUTIONS OF CADMIUM, ZINC, NICKEL, AND COPPER IN THE NORTH PACIFIC. Earth and Planetary Science Letters, 47(2): 176-198.
Brunauer, S., Emmett, P.H., Teller, E., 1936. Absorbtion of gases in multimolecular layers.
Cameron, V., Vance, D., 2014. Heavy nickel isotope compositions in rivers and the oceans. Geochimica Et Cosmochimica Acta, 128: 195-211.
Cameron, V., Vance, D., Archer, C., House, C.H., 2009. A biomarker based on the stable isotopes of nickel. Proceedings of the National Academy of Sciences of the United States of America, 106(27): 10944-10948.
Chukhrov, F.V., Gorshkov, A.I., Ermilova, L.P., Berezovskaya, V.V., Sivtsov, A.V., 1981. MINERAL FORMS OF MANGANESE AND IRON IN OCEANIC SEDIMENTS. Izvestiya Akademii Nauk Sssr Seriya Geologicheskaya(4): 5-21.
Ciscato, E.R., Bontognali, T.R.R., Vance, D., 2018. Nickel and its isotopes in organic-rich sediments: implications for oceanic budgets and a potential record of ancient seawater. Earth and Planetary Science Letters, 494: 239-250.
Cronan, D.S., 2000. Handbook of marine mineral deposits. CRC Press London.
Feller, C. et al., 1991. NATURE OF ORGANIC-MATTER ASSOCIATED WITH CLAYEY FRACTIONS OF A FERRALLITIC SOIL. Comptes Rendus De L Academie Des Sciences Serie Ii, 312(12): 1491-1497.
Fujii, T., Moynier, F., Dauphas, N., Abe, M., 2011. Theoretical and experimental investigation of nickel isotopic fractionation in species relevant to modern and ancient oceans. Geochimica Et Cosmochimica Acta, 75(2): 469-482.
Gaillardet, J., Viers, J., Dupre, B., 2014. Trace Elements in River Waters, Treatise on geochemistry, 2nd Edition. Elsevier, pp. 195-235.
Gall, L. et al., 2013. Nickel isotopic compositions of ferromanganese crusts and the constancy of deep ocean inputs and continental weathering effects over the Cenozoic. Earth and Planetary Science Letters, 375: 148-155.
Gueguen, B., Rouxel, O., Ponzevera, E., Bekker, A., Fouquet, Y., 2013. Nickel Isotope Variations in Terrestrial Silicate Rocks and Geological Reference Materials Measured by MC-ICP-MS. Geostandards and Geoanalytical Research, 37(3): 297-317.

Gueguen, B. et al., 2016. Comparative geochemistry of four ferromanganese crusts from the Pacific Ocean and significance for the use of Ni isotopes as paleoceanographic tracers. Geochimica Et Cosmochimica Acta, 189: 214-235.
Gueguen, B. et al., 2018. Variable Ni isotope fractionation between Fe-oxyhydroxides and implications for the use of Ni isotopes as geochemical tracers. Chemical Geology, 481: 38-52.
Horner, T.J. et al., 2010. Ferromanganese crusts as archives of deep water Cd isotope compositions. Geochemistry Geophysics Geosystems, 11.
Kashiwabara, T., Takahashi, Y., Tanimizu, M., Usui, A., 2011. Molecular-scale mechanisms of distribution and isotopic fractionation of molybdenum between seawater and ferromanganese oxides. Geochimica Et Cosmochimica Acta, 75(19): 5762-5784.
Kelly, S.D., Hesterberg, D., Ravel, B., 2008. Analysis of Soils and Minerals Using X-ray Absorption Spectroscopy, Methods of Soil Analysis. Soil Science Society of America, Madison, WI, pp. 387-463.
Konhauser, K.O. et al., 2009. Oceanic nickel depletion and a methanogen famine before the Great Oxidation Event. Nature, 458(7239): 750-U85.
Koschinsky, A., Halbach, P., 1995. Sequential leaching of marine ferromanganese precipitates: Genetic implications. Geochimica et Cosmochimica Acta, 59(24): 5113-5132.
Koschinsky, A., Hein, J.R., 2003. Uptake of elements from seawater by ferromanganese crusts: solid-phase associations and seawater speciation. Marine geology, 198: 331-351.
Langmuir, D., 1997. Aqueous environmental geochemistry. Prentice-Hall, Inc.
Lanson, B. et al., 2002. Structure of heavy-metal sorbed birnessite: Part 1. Results from X-ray diffraction. American Mineralogist, 87(11-12): 1631-1645.
Lemarchand, E., Schott, J., Gaillardet, J., 2007. How surface complexes impact boron isotope fractionation: Evidence from Fe and Mn oxides sorption experiments. Earth and Planetary Science Letters, 260(1-2): 277-296.
Lopano, C.L., Heaney, P.J., Post, J.E., 2009. Cs-exchange in birnessite: Reaction mechanisms inferred from time-resolved X-ray diffraction and transmission electron microscopy. American Mineralogist, 94(5-6): 816-826.
Mackey, D.J., 1983. METAL ORGANIC-COMPLEXES IN SEAWATER - AN INVESTIGATION OF NATURALLY-OCCURRING COMPLEXES OF CU, ZN, FE, MG, NI, CR, MN AND CD USING HIGH-PERFORMANCE LIQUID-CHROMATOGRAPHY WITH ATOMIC FLUORESCENCE DETECTION. Marine Chemistry, 13(3): 169-180.
Mackey, D.J., O'Sullivan, J.E., Watson, R.J., Dal Pont, G., 2002. Trace metals in the Western Pacific: temporal and spatial variability in the concentrations of Cd, Cu, Mn and Ni. Deep-Sea Research Part I-Oceanographic Research Papers, 49(12): 2241-2259.
Manceau, A., Kersten, M., Marcus, M.A., Geoffroy, N., Granina, L., 2007a. Ba and Ni speciation in a nodule of binary Mn oxide phase composition from Lake Baikal. Geochimica Et Cosmochimica Acta, 71(8): 1967-1981.
Manceau, A., Lanson, B., Drits, V., 2002a. Structure of heavy metal sorbed birnessite. Part III: Results from powder and polarized extended x-ray absorption fine structure spectroscopy. Geochim. Cosmochim. Acta, 66(15): 2639-2663.
Manceau, A., Lanson, B., Drits, V.A., 2003. Structure of heavy metal sorbed birnessite. Part III: Results from powder and polarized EXAFS spectroscopy. (vol 66, pg 2639, 2002). Geochimica Et Cosmochimica Acta, 67(8): 1599-1599.
Manceau, A., Lanson, M., Geoffroy, N., 2007b. Natural speciation of Ni, Zn, Ba, and As in ferromanganese coatings on quartz using X-ray fluorescence, absorption, and diffraction. Geochimica Et Cosmochimica Acta, 71(1): 95-128.

Manceau, A., Lason, M., Geoffroy, N., 2007c. Natural speciation of Ni, Zn, Ba, and As in ferromanganese coatings on quartz using X-ray fluorescence, absorption, and diffraction. Geochim Cosmochim Acta, 71: 95-128.

Manceau, A. et al., 2002b. Deciphering Ni sequestration in soil ferromanganese nodules by combining x-ray fluorescence, absorption, and diffraction at micrometer scales of resolution. American Mineralogist, 87(10): 1494-1499.

McKenzie, R.M., 1971. The synthesis of birnessite, cryptomelane, and some other oxides and hydroxides of manganese. Mineral. Mag., 38: 493-502.

Morel, F.M.M., Milligan, A.J., Saito, M.A., 2003. Marine bioinorganic chemistry: the role of trace metals in the oceanic cycles of major nutrients, Treatise on Geochemistry. Elsevier, pp. 113-143.

Morel, F.M.M., Price, N.M., 2003. The biogeochemical cycles of trace metals in the ocean. Science, 300: 944-947.

Nicholson, K., Eley, M., 1997. Geochemistry of manganese oxides: metal adsorption in freshwater and marine environments. In: Nicholson, K., Hein, J.R., Bühn, B., Dasgupta, S. (Eds.), Manganese Mineralization: Geochemistry and Mineralogy of Terrestrial and Marine Deposits. Geological Society Special Publication No. 119. The Geological Society, London, pp. 309-326.

Nielsen, S.G. et al., 2013. Towards an understanding of thallium isotope fractionation during adsorption to manganese oxides. Geochimica Et Cosmochimica Acta, 117: 252-265.

Nimmo, M., Van Den Berg, C.M.G., Brown, J., 1989. THE CHEMICAL SPECIATION OF DISSOLVED NICKEL, COPPER, VANADIUM AND IRON IN LIVERPOOL BAY, IRISH SEA. Estuarine Coastal and Shelf Science, 29(1): 57-74.

NIST, 1995. Critical Stability Constants of Metal Complexes Database. National Institute of Standards and Technology (NIST).

Peacock, C.L., 2009. Physiochemical controls on the crystal-chemistry of Ni in birnessite: Genetic implications for ferromanganese precipitates. Geochim Cosmochim Acta, 73: 3568-3578.

Peacock, C.L., Sherman, D.M., 2005. Copper(II) sorption onto goethite, hematite, and lepidocrocite: A surface complexation model based on ab initio molecular geometries and EXAFS spectroscopy (vol 68, pg 2623, 2004). Geochimica Et Cosmochimica Acta, 69(21): 5141-5142.

Peacock, C.L., Sherman, D.M., 2007a. Crystal-chemistry of Ni in marine ferromanganese crusts and nodules. Amer. Mineral., 92: 1087-1092.

Peacock, C.L., Sherman, D.M., 2007b. Sorption of Ni by birnessite: Equilibrium controls on Ni in sewater. Chem Geol, 238: 94-106.

Pena, J., Bargar, J.R., Sposito, G., 2011. Role of bacterial biomass in the sorption of Ni by biomass-birnessite assemblages. Environmental Science & Technology, 45: 7338-7344.

Pena, J., Kwon, K.D., Refson, K., Bargar, J.R., Sposito, G., 2010. Mechanisms of nickel sorption by a bacteriogenic birnessite. Geochim Cosmochim Acta, 74: 3076-3089.

Pokrovsky, O.S., Galy, A., Schott, J., Pokrovski, G.S., Mantoura, S., 2014. Germanium isotope fractionation during Ge adsorption on goethite and its coprecipitation with Fe oxy(hydr)oxides. Geochimica Et Cosmochimica Acta, 131: 138-149.

Pokrovsky, O.S., Viers, J., Freydier, R., 2005. Zinc stable isotope fractionation during its adsorption on oxides and hydroxides. Journal of Colloid & Interface Science, 291: 192-200.

Porter, S.J., Selby, D., Cameron, V., 2014. Characterising the nickel isotopic composition of organic-rich marine sediments. Chemical Geology, 387: 12-21.

Post, J.E., Veblen, D.R., 1990. Crystal structure determinations of synthetic sodium, magnesium, and potassium birnessite using TEM and the Rietveld method. American Mineralogist, 75: 477-489.

Ratie, G. et al., 2015. Nickel isotope fractionation during tropical weathering of ultramafic rocks. Chemical Geology, 402: 68-76.

Ravel, B., Newville, M., 2005. Athena, Artemis, Hephaestus: data analysis for X-ray absorption spectroscopy using IFEFFIT. Journal of Synchrotron Radiation, 12: 537-541.
Rothman, D.H. et al., 2014. Methanogenic burst in the end-Permian carbon cycle. Proceedings of the National Academy of Sciences of the United States of America, 111(15): 5462-5467.
Schmitt, A.D., Galer, S.J.G., Abouchami, W., 2009. Mass-dependent cadmium isotopic variations in nature with emphasis on the marine environment. Earth and Planetary Science Letters, 277(1-2): 262-272.
Sclater, F.R., Boyle, E., Edmond, J.M., 1976. MARINE GEOCHEMISTRY OF NICKEL. Earth and Planetary Science Letters, 31(1): 119-128.
Siebert, C., Nagler, T.F., Kramers, J.D., 2001. Determination of molybdenum isotope fractionation by double-spike multicollector inductively coupled plasma mass spectrometry. Geochemistry Geophysics Geosystems, 2: art. no.-2000GC000124.
Silvester, E., Manceau, A., Drits, V.A., 1997. Structure of synthetic monoclinic Na-rich birnessite and hexagonal birnessite: II. Results from chemical studies and EXAFS spectroscopy. Am. Mineral., 82: 962-978.
Simanova, A.A. et al., 2015. Probing the sorption reactivity of the edge surfaces in birnessite nanoparticles using nickel(II). Geochimica Et Cosmochimica Acta, 164: 191-204.
Sposito, G., 1989. The chemistry of soils. Oxford University Press, New York, New York, 277 pp.
Takahashi, Y., Manceau, A., Geoffroy, N., Marcus, M.A., Usui, A., 2007. Chemical and structural control of the partitioning of Co, Ce, and Pb in marine ferromanganese oxides. Geochim Cosmochim Acta, 71: 984-1008.
Toner, B., Manceau, A., Marcus, M.A., Millet, D.B., Sposito, G., 2005. Zn sorption by a bacterial biofilm. Environ Sci Technol, 39: 8288-8294.
Toner, B., Manceau, A., Webb, S.M., Sposito, G., 2006. Zinc sorption to biogenic hexagonal-birnessite particles within a hydrated bacterial biofilm. Geochim. Cosmochim. Acta, 70: 27-43.
Turner, A., Martino, M., 2006. Modelling the equilibrium speciation of nickel in the Tweed Estuary, UK: Voltammetric determinations and simulations using WHAM. Marine Chemistry, 102(3-4): 198-207.
Turner, A., Nimmo, M., Thuresson, K.A., 1998. Speciation and sorptive behaviour of nickel in an organic-rich estuary (Beaulieu, UK). Marine Chemistry, 63(1-2): 105-118.
Van den Berg, C.M.G., Nimmo, M., 1987. Determination of interactions of nickel with dissolved organic material in seawater using cathodic stripping voltammetry. Science of the Total Environment, 60: 185-195.
Vance, D., Archer, C., Little, S.H., Kobberich, M., de Souza, G.F., 2017. The oceanic cycles of the transition metals and their isotopes. Acta Geochimica, 36(3): 359-362.
Vance, D. et al., 2016. The oceanic budgets of nickel and zinc isotopes: the importance of sulfidic environments as illustrated by the Black Sea. Philosophical Transactions of the Royal Society a-Mathematical Physical and Engineering Sciences, 374(2081).
Villalobos, M., Lanson, B., Manceau, A., Toner, B., Sposito, G., 2006. Structural model for the biogenic Mn oxide produced by *Pseudomonas putida*. Am. Mineral., 91: 489-502.
Villalobos, M., Toner, B., Bargar, J., Sposito, G., 2003. Characterization of the manganese oxide produced by *Pseudomonas putida* strain MnB1. Geochim. Cosmochim. Acta, 67(14): 2649-2662.
Wasylenki, L.E., Howe, H.D., Spivak-Birndorf, L.J., Bish, D.L., 2015. Ni isotope fractionation during sorption to ferrihydrite: Implications for Ni in banded iron formations. Chemical Geology, 400: 56-64.
Wasylenki, L.E., Swihart, J.W., Romaniello, S.J., 2014. Cadmium isotope fractionation during adsorption to Mn oxyhydroxide at low and high ionic strength. Geochimica Et Cosmochimica Acta, 140: 212-226.

Webb, S.M., 2005. SIXPACK: A graphical user interface for XAS analysis using IFEFFIT. Physica Scripta, T115: 1011-1014.

Table 1 Ni sorption

Experiment Groups	Sample Name	pH	$[Ni]_{aq}^{initial}$ (µmol / L)	Final loading to mineral (µmol Ni/g)	Final loading to mineral (µmol Ni/m^2)	% of Ni sorption[e]	$\delta^{60/58}Ni_{mineral}$ (mineral)	[d]2se	$\delta^{60/58}Ni_{aqueous}$ (aqueous)	2se	$\Delta^{60/58}Ni_{min-aq}$ (mineral - aqueous)	2se	Calculated $\delta^{60/58}Ni_{initial}$ [f]	Ni EXAFS data collected
[a]pH gradient - set 1	NiBirn_pH50_C227	5	170	227	6,28	99,7	-0,33	0,02	[e]-	-	-	-	-	yes
	NiBirn_pH60_C234	6	170	234	6,47	99,9	-0,35	0,02	-	-	-	-	-	yes
	NiBirn_pH70_C222	7	170	222	6,14	99,9	-0,35	0,02	-	-	-	-	-	yes
	NiBirn_pH80_C227	8	170	227	6,30	99,9	-0,32	0,03	-	-	-	-	-	yes
[b]Concentration gradient	NiBirn_pH77_C021	7,7	17	21,5	0,60	99,7	-0,29	0,03	-	-	-	-	-	yes
	NiBirn_pH77_C110	7,7	85	110	3,06	100,0	-0,37	0,06	-	-	-	-	-	no
	NiBirn_pH77_C225	7,7	170	225	6,22	99,9	-0,34	0,02	-	-	-	-	-	no
	NiBirn_pH77_C189	7,7	341	189	5,24	71,4	-1,05	0,02	-	-	-	-	-	yes
	NiBirn_pH77_C190	7,7	426	190	5,25	64,0	-1,17	0,03	-	-	-	-	-	yes
[c]pH gradient - set 2	NiBirn_pH60_C253	6	170	254	7,02	59,5	-1,43	0,03	1,33	0,03	-2,76	0,04	-0,31	yes
	NiBirn_pH70_C246	7	170	246	6,82	68,0	-1,41	0,04	1,94	0,04	-3,35	0,05	-0,34	yes
	NiBirn_pH77_C113	7,7	170	113	3,12	62,5	-1,45	0,02	1,58	0,04	-3,04	0,05	-0,31	yes
	NiBirn_pH77_C244	7,7	170	244	6,76	63,4	-1,53	0,03	1,56	0,04	-3,09	0,05	-0,40	no
	NiBirn_pH80_C239	8	170	239	6,62	60,7	-1,51	0,03	1,53	0,05	-3,04	0,06	-0,32	no
	NiBirn_pH80_C250	8	170	250	6,91	59,7	-1,52	0,03	1,37	0,05	-2,88	0,06	-0,35	yes
	NiBirn_pH82_C249	8,2	170	249	6,88	59,9	-1,37	0,02	1,40	0,03	-2,77	0,04	-0,26	yes
	Ni standard solution	-	-	-	-	-	-	-	-0,32	0,03	-	-	-	

a Experiments having variable pH, constant dissolved Ni concentration, and 0.15 g hexagonal birnessite per reactor
b Experiments having variable dissolved Ni concentration, constant pH, and 0.15 g hexagonal birnessite per reactor
c Experiments having variable pH, constant dissolved Ni concentration, and 0.075 g hexagonal birnessite per reactor
d Standard deviation
e "-" not anlaysed
f This calculation was done by mass balance.

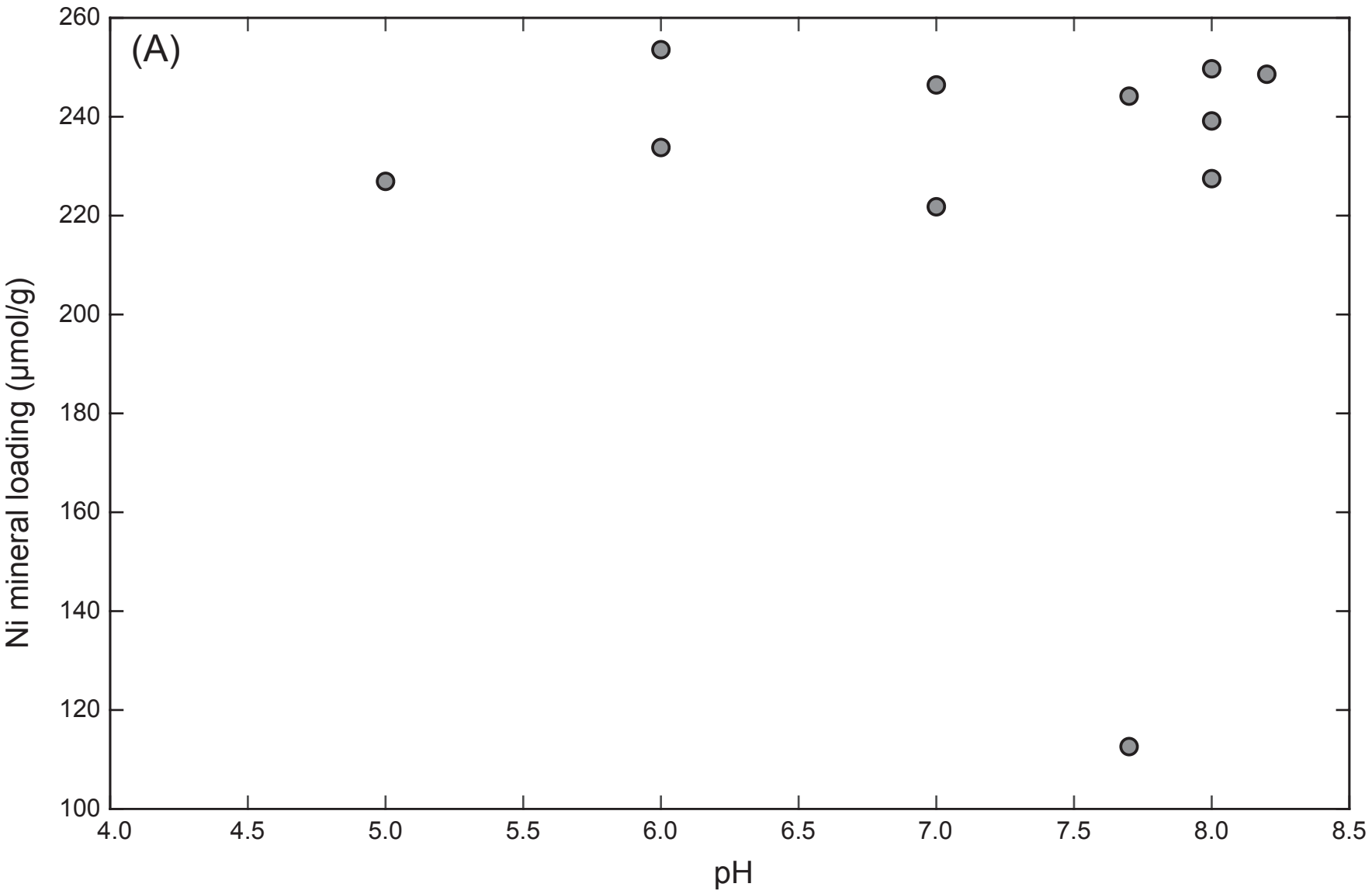
(A)
Ni mineral loading (µmol/g)
260
240
220
200
180
160
140
120
100
4.0
4.5
5.0
5.5
6.0
6.5
7.0
7.5
8.0
8.5
pH

(B)
Ni mineral loading (µmol/g)
250
200
150
100
50
0
0
50
100
150
200
250
300
350
400
450
Ni initial concentration (µmol/L)

Figure 1

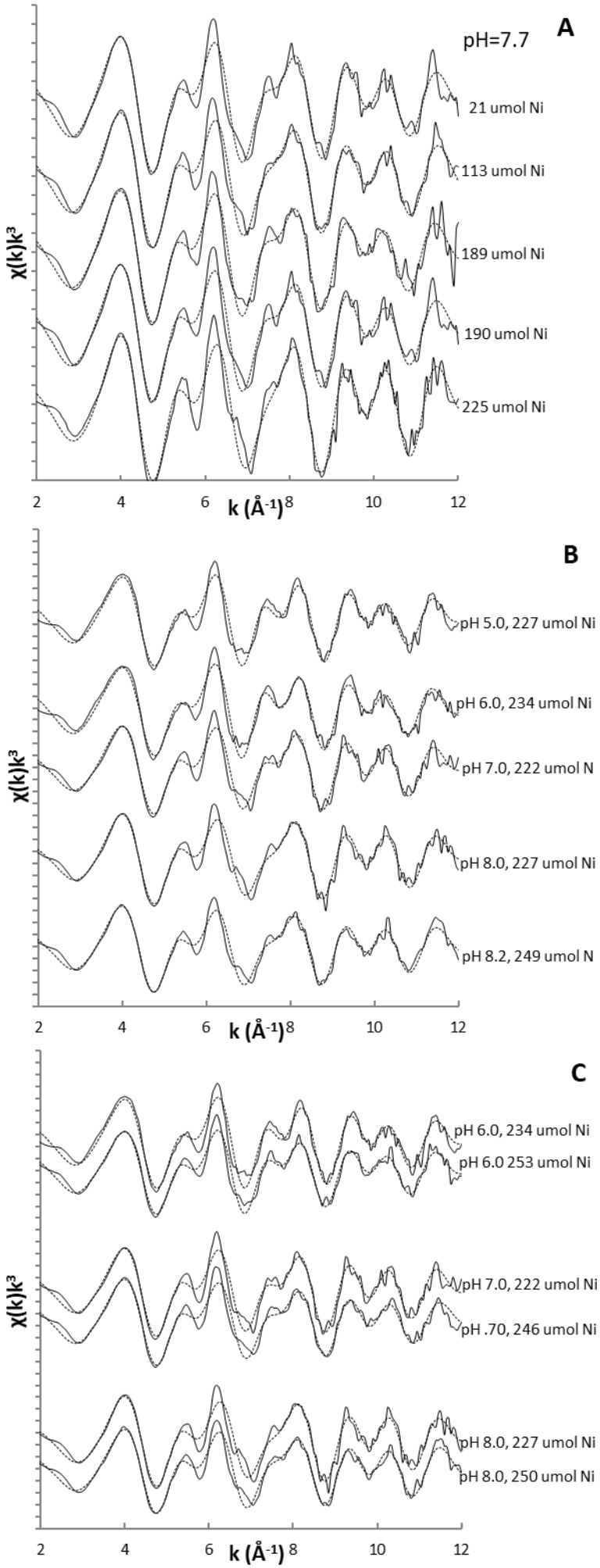
A
pH=7.7
21 umol Ni
113 umol Ni
189 umol Ni
190 umol Ni
225 umol Ni
χ(k)k³
2
4
6
k (Å⁻¹)
8
10
12
B
pH 5.0, 227 umol Ni
pH 6.0, 234 umol Ni
pH 7.0, 222 umol N
pH 8.0, 227 umol Ni
pH 8.2, 249 umol N
χ(k)k³
2
4
6
k (Å⁻¹)
8
10
12
C
pH 6.0, 234 umol Ni
pH 6.0 253 umol Ni
pH 7.0, 222 umol Ni
pH .70, 246 umol Ni
pH 8.0, 227 umol Ni
pH 8.0, 250 umol Ni
χ(k)k³
2
4
6
k (Å⁻¹)
8
10
12

Figure 2

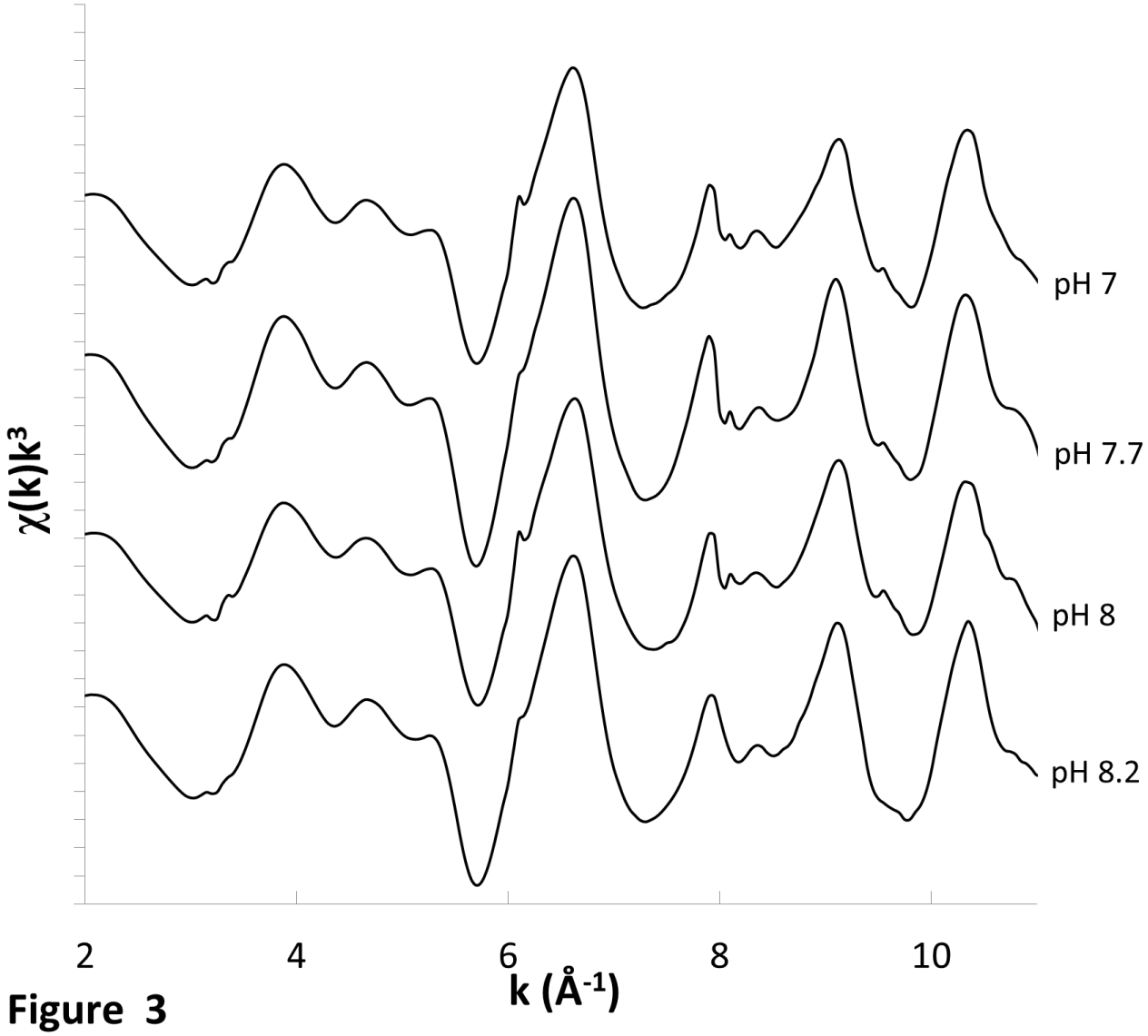

Figure 3

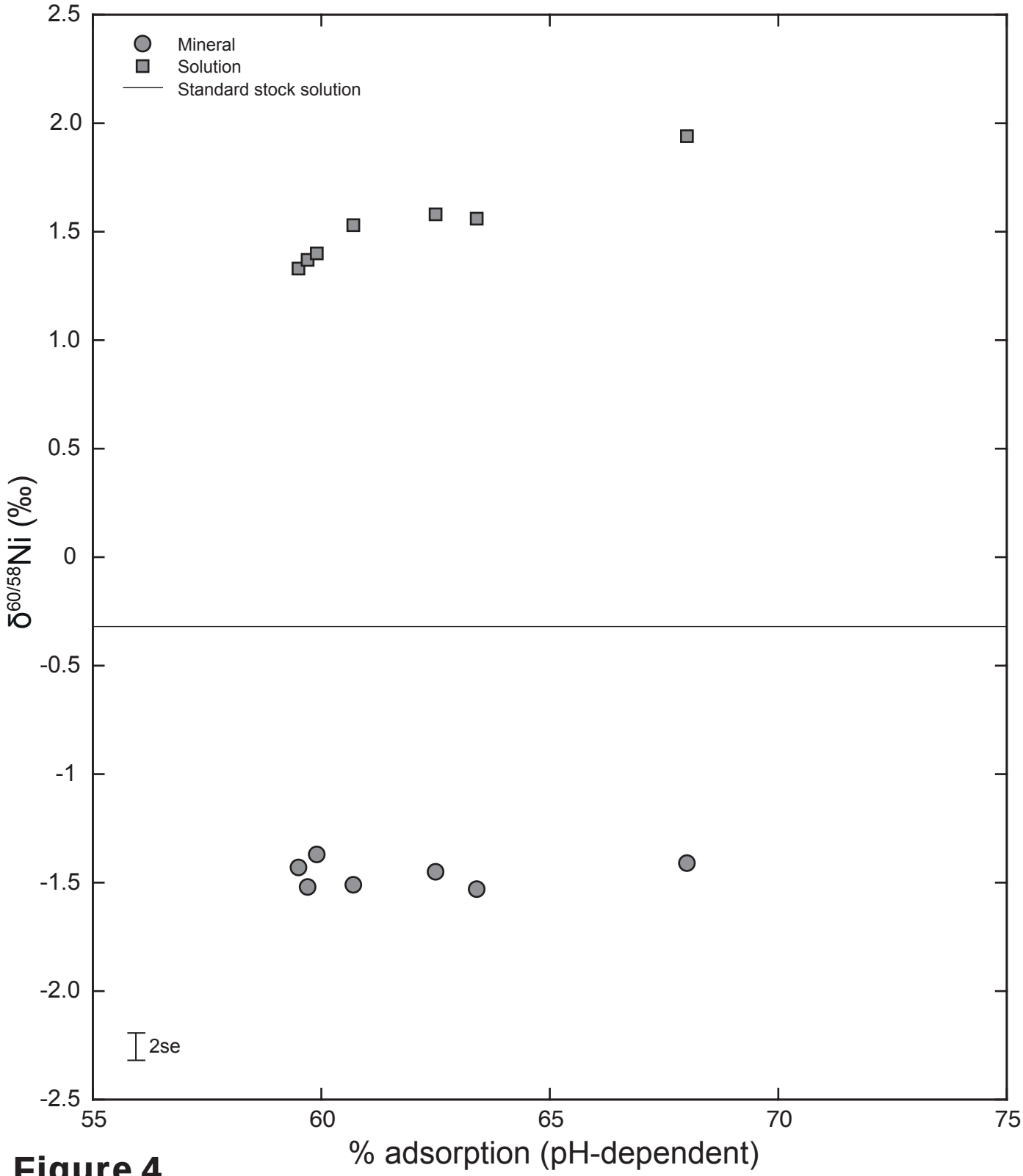
Mineral
Solution
Standard stock solution
2.5
2.0
1.5
1.0
0.5
0
-0.5
-1
-1.5
-2.0
-2.5
δ60/58Ni (‰)
2se
55
60
65
70
75
% adsorption (pH-dependent)

Figure 4

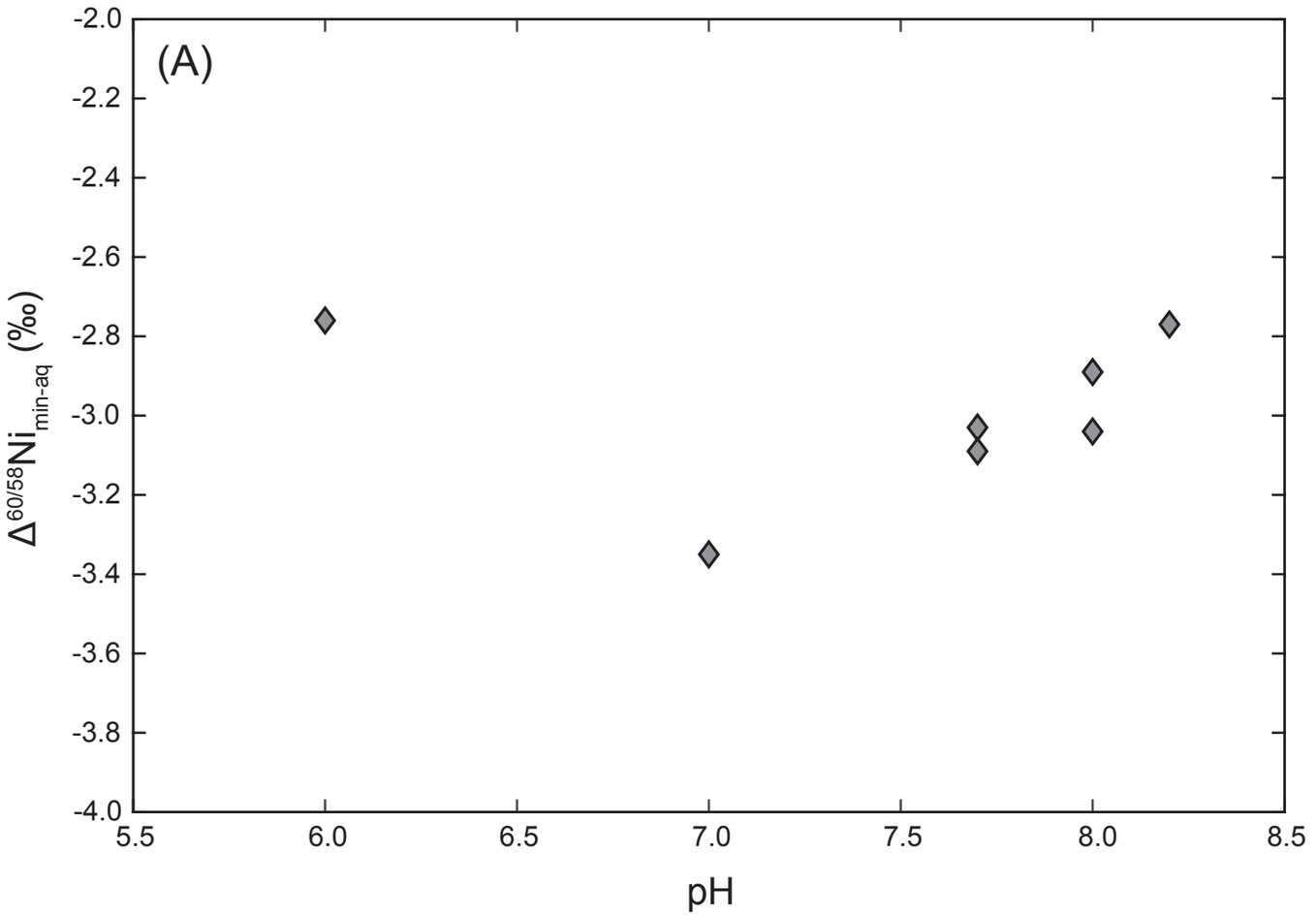
(A)
-2.0
-2.2
-2.4
-2.6
-2.8
-3.0
-3.2
-3.4
-3.6
-3.8
-4.0
$\Delta^{60/58}Ni_{min\text{-}aq}$ (‰)
5.5
6.0
6.5
7.0
7.5
8.0
8.5
pH

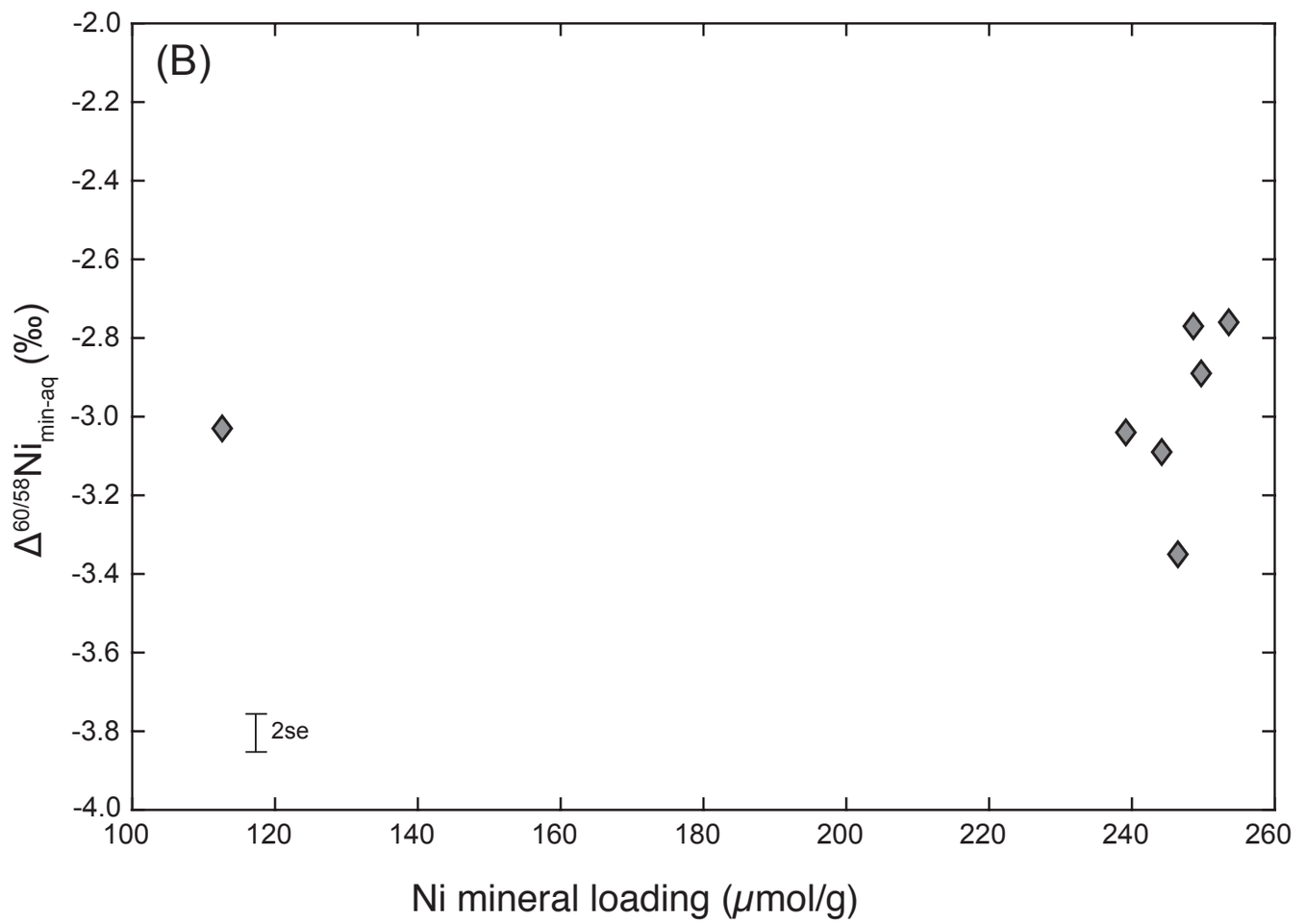
(B)
-2.0
-2.2
-2.4
-2.6
-2.8
-3.0
-3.2
-3.4
-3.6
-3.8
-4.0
$\Delta^{60/58}Ni_{min\text{-}aq}$ (‰)
2se
100
120
140
160
180
200
220
240
260
Ni mineral loading (μmol/g)

Figure 5

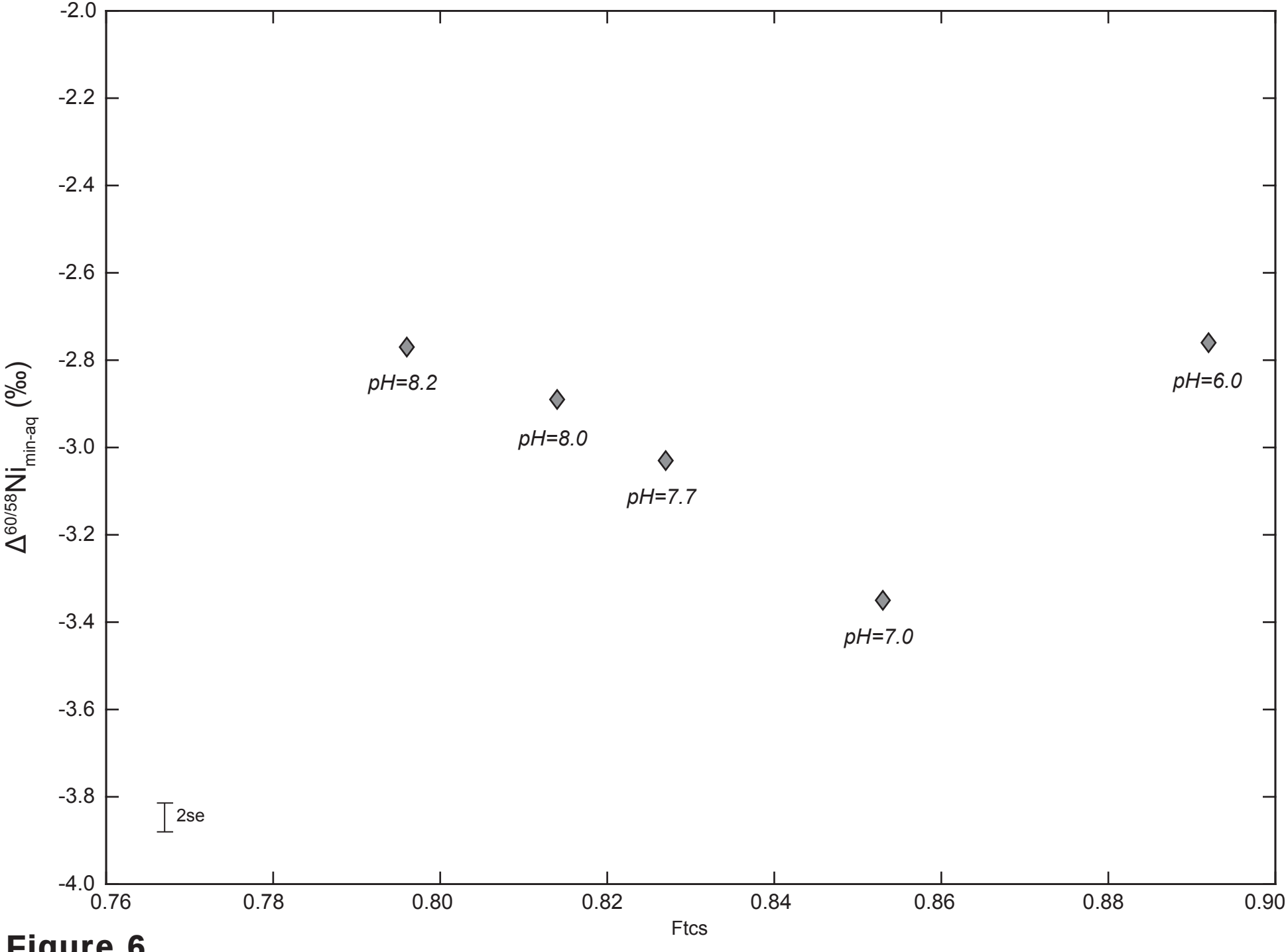
-2.0
-2.2
-2.4
-2.6
-2.8
-3.0
-3.2
-3.4
-3.6
-3.8
-4.0
$\Delta^{60/58}Ni_{min\text{-}aq}$ (‰)
0.76
0.78
0.80
0.82
0.84
0.86
0.88
0.90
Ftcs
pH=8.2
pH=8.0
pH=7.7
pH=7.0
pH=6.0
2se

Figure 6